Dendritic and Synaptic Effects in the Hippocampus of Rats Acutely Intoxicated with Diisopropylfluorophosphate

By

JASON W. LOXTERKAMP

THESIS

Submitted in partial satisfaction of the requirements for the degree of

MASTER OF SCIENCE

in

Forensic Science

in the

OFFICE OF GRADUATE STUDIES

of the

UNIVERSITY OF CALIFORNIA

DAVIS

Approved:

Pamela J. Lein, Chair

Abhijit J. Chaudhari

James M. Angelastro

Committee in Charge

2022

Dendritic and Synaptic Effects in the Hippocampus of Rats Acutely Intoxicated with Diisopropylfluorophosphate

Authors: Jason W Loxterkamp[1], Brad A. Hobson[2], Naomi Saito[3], Danielle J. Harvey[3], Abhijit J. Chaudhari[2,4], Pamela J. Lein[1]

[1]Department of Molecular Biosciences, University of California, Davis, School of Veterinary Medicine, Davis, CA 95616; [2]Center for Molecular and Genomic Imaging, University of California, Davis, College of Engineering, Davis, CA 95616; [3]Department of Public Health Sciences, University of California, Davis, School of Medicine, California 95616; [4]Department of Radiology, University of California, Davis, School of Medicine, California 95616

Highlights

- Complexity of distal basilar dendrites was increased at 10 days post-DFP exposure
- MAP2 immunoreactivity was decreased at 10 and 28 days post-DFP exposure
- DFP intoxication did not significantly alter dendritic spine or synaptic density
- Synaptic plasticity may be altered at delayed times post-DFP exposure
- Quantitative SV2A PET measures and spine density were positively correlated

Keywords: Golgi stain, immunohistochemistry, Magnetic Resonance Imaging, MAP2, organophosphates, Positron Emission Tomography, PSD95, SV2A, *Status Epilepticus*

Abstract:

Individuals who survive the cholinergic crisis triggered by acute intoxication with organophosphate (OP) cholinesterase inhibitors often experience chronic morbidity, including cognitive deficits, depression and anxiety, and spontaneous recurrent seizures. The pathogenic mechanisms that link the acutely toxic effects of OPs to chronic neurological outcomes remain speculative. One potential mechanism is altered synaptic connectivity as a result of changes in dendritic morphology. While acute OP intoxication has been reported to alter dendritic morphology in the hours after exposure, whether these effects persist at more delayed times post-exposure is not known. Here, we address this data gap by testing the hypothesis that acute OP intoxication causes persistent changes in the cytoarchitecture of dendrites and synapses. To test our hypothesis, adult male Sprague-Dawley rats (200-250 g) were administered a single dose of diisopropylfluorophosphate (DFP; 4 mg/kg s.c.) or vehicle (VEH; saline) followed 1 min later by atropine sulfate (2 mg/kg i.m.) and 2-pralidoxime (25 mg/kg i.m.). All DFP-intoxicated rats (n = 28) exhibited characteristic signs of cholinergic crisis (i.e., SLUD: salivation, lacrimation, urination, defecation) and seizure behavior within minutes after exposure. Analysis of Golgi-stained pyramidal neurons and quantitative immunohistochemistry (IHC) of synaptic vesicle glycoprotein 2A (SV2A), postsynaptic density protein 95 (PSD95), and microtubule associated protein 2 (MAP2), were used to characterize the effects of acute OP intoxication on dendrites and synapses at 10 and 28 days post exposure (DPE). Golgi-stained pyramidal neurons in the CA1 hippocampus of DFP animals displayed increased arborization of basilar dendrites at 10 DPE but no changes relative to vehicle controls were seen at 28 DPE. DFP animals showed no changes in dendritic spine density at either time post-exposure, but at both times, the percentage of spines with immature morphology (filopodia) was increased. Quantitative IHC revealed decreased MAP2 immunoreactivity (IR) but no significant differences in synapses in the CA1 hippocampus of DFP animals at 10 and 28 DPE. Since histologic techniques do not allow for longitudinal measurements and cannot be translated to clinical

evaluation of human survivors, we also evaluated *in vivo* positron emission tomography (PET) for quantifying SV2A binding as an approach for assessing synaptic density. DFP animals displayed no significant difference in the SV2A binding in the whole hippocampus relative to vehicle controls as assessed by PET standardized uptake value (SUV), but there was a significant correlation with histological assessments of synapses. These findings support the hypothesis that altered dendritic morphology, notably increased dendritic complexity of individual neurons but decreased regional MAP2 IR at 10 DPE, contributes to the chronic morbidity associated with acute OP intoxication. This study also revealed that global assessments of synaptic density by PET are positively correlated with histologic measures, suggesting that further exploration of SV2A PET as an approach for assessing synaptic density in human survivors of acute OP intoxication is warranted.

Introduction:

Acute intoxication with organophosphate (OP) cholinesterase inhibitors can result in seizures that quickly progress to life-threatening *status epilepticus* (SE) [1]. This toxidrome is often fatal if not rapidly treated with atropine to block muscarinic receptors, oxime to reactivate acetylcholinesterase, and benzodiazepines to reduce seizure activity [1, 2]. Individuals who survive OP-induced SE exhibit significant morbidity, including cognitive deficits, depression and anxiety, and spontaneous recurrent seizures (SRS)[3]. As such, OPs remain a public health concern, especially with their widespread use as pesticides and employment as warfare agents as recently as 2020 [4].

The pathogenic mechanisms that link the acute and chronic neurotoxic effect of OP intoxication remain a significant focus of research. Military and civilian laboratories have used preclinical models to evaluate candidates for mitigating the long term neurologic effects associated with OP-induced SE. The OP pesticide diisopropylfluorophosphate (DFP) is widely used in these models due to its availability and its structural and functional similarities to OP warfare agents. Although the toxic effects profile of each OP is chemically distinct in terms of potency and response to therapeutics [5], the toxic mechanisms of action and pathologic effects of OPs are conserved. Thus, rat models of acute DFP intoxication are a relevant model for characterizing the mechanism(s) contributing to the chronic morbidity of acute OP intoxication [5-7]. For these studies we leveraged a rat model of acute DFP intoxication that has been demonstrated to recapitulate the acute and chronic neurotoxicity observed in humans acutely intoxicated with OPs, including severe acute seizure behavior, neurodegeneration, activation of the neuroinflammatory response, spontaneous recurrent seizures, and deficits in learning and memory [8-11].

Altered synaptic connectivity is hypothesized to contribute to the pathogenesis of the chronic neurotoxic effects of acute OP intoxication. It is well-established that altered synaptic connectivity is

associated with neurological diseases that are characterized by electrographic abnormalities [12-14], cognitive dysfunction [15-17], and affective disorders [18-20]; morbidities described in human and animal survivors of acute OP intoxication. For example, decreased synaptic density or connectivity is observed in the early phase after SE and is followed by a later phase during which synaptic density recovers to levels approaching basal levels [13, 14]. A few laboratories have investigated the effects of acute intoxication with the OPs soman, DFP, or paraoxon on neuronal and synaptic connectivity and found significantly decreased dendritic spine density [21-23], total dendritic length [23], and presynaptic protein levels [24] in CA1 neurons. However, data from these studies are limited to the first 24 hours after OP-induced SE. It remains unknown what effects acute OP intoxication has on dendrites or synapses at times beyond this early phase subsequent to exposure. Models of chronic exposure to OPs at levels that do not trigger cholinergic crisis or SE similarly demonstrate an early phase of synaptic deterioration and provide a glimpse into effects of OPs at times past the initial 24 hours post-exposure [25-28]. A biphasic progression of synaptic alterations was observed *in vivo* following repeated subclinical OP exposure, marked by an increase in electrographic synaptic transmission in the first week followed by a decrease in both synaptic transmission and dendritic spine density 3 months after exposure [28].

In the present study, we hypothesized that the effects of acute OP intoxication on dendritic and synaptic connectivity would persist to later times post-exposure. To test this hypothesis, dendritic and synaptic effects were assessed at in a rat model of acute DFP intoxication at 10 and 28 days post exposure (DPE), and the effects were quantified with gold standard histological techniques as well as longitudinally measured by *in vivo* positron emission tomography (PET). PET radiotracers specific to synaptic vesicle glycoprotein 2A (SV2A), a membrane protein expressed in neurons and endocrine cells and involved in the regulation of neurotransmitter release, were used to quantify *in vivo* synaptic effects [29]. While Golgi staining and quantitative immunohistochemistry (IHC) with markers of SV2A,

postsynaptic density protein 95 (PSD95), microtubule associated protein 2 (MAP2) were used further characterized these effects.

Materials and Methods:

1. Animals and Exposures

All experiments involving animals complied with the ARRIVE guidelines and were reviewed and approved by the University of California, Davis, Institutional Animal Care and Use Committee (IACUC). Adult male Sprague-Dawley rats (200-250 g, Charles River Laboratories, Hollister, CA) were administered a single dose of DFP (4 mg/kg, s.c.) or vehicle (VEH; saline) followed 1 min later by atropine sulfate (2 mg/kg, i.m.) and 2-pralidoxime (25 mg/kg, i.m.). A modified Racine scale was used to score behavioral seizure activity every 5 to 20 min for the first 240 min post-DFP as previously described [30]. Only DFP rats that achieved a maximal score of $\geq$ 3 and an average seizure score of $\geq$ 2.5 over the 240 min of seizure scoring were included in the study. At the end of the 240 min observation period animals were injected s.c. with 10 ml 5% dextrose in 0.9% isotonic saline (Baxter International, Deerfield, IL, USA) prior to being returned to their home cages. Animals were provided access to moistened chow until they resumed consumption of solid chow. At the conclusion of the seizure scoring, all animals were individually housed in standard plastic shoebox cages in facilities fully accredited by AAALAC International under controlled environmental conditions (22 ± 2 °C, 40–50% humidity, and a 12 h light-dark cycle). Food and water were provided *ad libitum*.

2. Tissue Preparation

At the conclusion of *in vivo* imaging (PET and MRI), animals were returned to the vivarium for 24 hours to allow the PET radiotracer to radioactively decay to background (at least 10 radioactive half-lives). Once safe to handle, animals were deeply anesthetized with 4% isoflurane in medical grade oxygen, and

subsequently transcardially perfused with 100 ml cold phosphate-buffered saline (PBS; 3.6 mM Na_2HPO_4, 1.4mM NaH_2PO_4, 150mM NaCl, pH 7.2)) at a flow rate of 15 mL/min using a Masterflex peristaltic pump (Cole Parmer, Vernon Hills, IL, USA). The brain of each animal was removed and hemisected. The left hemisphere was processed for Golgi staining and the right hemisphere for immunohistochemistry.

3. Golgi Staining

3.1: Staining SOP and Vibratome Sectioning

Golgi staining was performed using the FD Rapid GolgiStain kit (FD NeuroTechnologies Inc., Columbia, MD) according to the manufacturer's instructions and as previously described [31, 32] with the following modifications. The hemisected left hemisphere of each brain was cut at the optic nerve chiasm before being placed in premixed Solutions A and B. After immersion in Solution C, brains were transferred to 10% (w/v) sucrose (Thermo Fisher Healthcare, Waltham, MA, USA) in PBS for 4 h at 4 ^{o}C and then stored in 30% (w/v) sucrose in PBS at 4 ^{o}C until sectioned. Brains were sliced into 100-µm thick coronal sections using a vibratome (VT-1000S, Leica, Solms, Germany), collecting about 30 slices per animal from ~-5.5 to ~-2.5 mm Bregma that were mounted on gelatin subbed slides. Slides were dried for a maximum of 1 week at room temperature (RT) in the dark. Next, sections were stained with Solutions D and E, dehydrated, and cleared following the FD Rapid GolgiStain kit instructions and coverslipped with Permount™ Mounting Medium (Thermo Fisher Scientific, Waltham, MA, USA).

3.2: Brightfield Image Acquisition

Golgi-stained sections were screened for pyramidal neurons in the CA1 hippocampus that met criteria for selection for Golgi analyses, as previously described including a) well-impregnated neurons with no evidence of incomplete or artificial staining, b) blood vessels, glia, or non-descript precipitate did not obscure neuron or branches, and c) the cell body was located in the middle third of the thickness of the

section [32]. Due to congestion of Golgi impregnated cells in the CA1, neurons with some overlapping branches that were still clearly resolved from neighboring branches were included. Slices were observed with an IX-81 inverted microscope (Olympus, Shinjuku, Japan) and screened for viable neurons starting from the most caudal slice and moving rostral. Serial image stacks of Golgi stained CA1 pyramidal neurons ($n \geq 5$ neurons per animal) were acquired using MetaMorph Image Analysis Software (version 7.8.11.0, Molecular Devices, Sunnyvale, CA) by an individual blinded to the groups. For each neuron, separate image stacks were acquired of the whole basilar dendritic arbor using a 20X objective lens (Olympus LUCPlanFLN 20x/0.45na Dry) while dendritic spines were imaged using a 60X objective lens (Olympus UPLANFLN 60x/1.25na Oil Iris). Serial image stacks of selected neurons were captured on a CCD camera (1392 x 1040 pixels) with a 1 ms exposure time. Each image series captured a total z-distance of ~50 µm of the tissue with a z-step of 0.2 µm.

3.3: Neurolucida Analysis of the Basal Dendritic Arbor

Basilar dendritic arbors were traced by an individual blinded to the groups using Neurolucida software (version 2019.1.4, MBF Bioscience, Williston, VT). Arbor complexity was quantified by branch structure analysis and Sholl analysis using Neurolucida Explorer software (version 2019.2.1, MBF Bioscience) as described previously [33]. Arbor complexity was further quantified by analyzing the area under the curve (AUC) for the total (0-280 µm), proximal (0-70 µm), and distal (70-280 µm) portions of the Sholl plots.

3.4: RECONSTRUCT Quantitative Analysis of Dendritic Spines

Image stacks of dendritic spines were pre-processed using FIJI 1.53c software (FIJI is Just ImageJ; https://imagej.net/Fiji; NIH) with the Concentric Circles plug-in to overlay concentric circles 50, 62.5, 75, 87.5, and 100 µm from the center of the cell body. Dendritic spines were traced by an individual blinded to the groups using RECONSTRUCT software (http://synapses.clm.utexas.edu) [34]. The criteria for

selecting dendritic segments included a) well-impregnated dendrites with no evidence of incomplete or artificial staining, b) blood vessels, glia, or non-descript precipitate did not obscure any dendritic spines, c) segments were between concentric circles located 50-75 (10 DPE) or 75-100 µm (28 DPE) from the neuronal cell body, d) segments were at least 5-7 µm from any bifurcations, and e) primary branches were excluded. Two to three dendritic segments (25-35 µm) were traced for each neuron. Dendritic spine identification criteria included any logical protrusion off the dendritic process that had a logical spine head and noticeable neck. Spine length and head width were systematically traced as previously described (Risher et al., 2014). Dendritic spine densities were quantified as the number of spines per 10 µm of dendrite length and qualitatively assessed for spine morphology using the template spreadsheet (Spreadsheet S1) provided by [35]. Dendritic spine morphology was characterized from length and width measurements, and spines were grouped into morphological types commonly found on pyramidal neurons, which include, in order of increasing maturity, filopodia, long thin, thin, stubby, and mushroom.

4. Immunohistochemistry:

4.1: Staining Standard Operating Procedure

Right brain hemispheres were blocked into 2-mm thick coronal sections and post-fixed in 4% (w/v) paraformaldehyde (Sigma; St. Louis, MO, USA) in 0.2 mM phosphate buffer for 24 h at 4 °C. After fixation, sections were incubated in 30% (w/v) sucrose (Thermo Fisher Healthcare) in PBS and stored at 4 °C for at least 48 h. Next, sections containing rostral, medial, and caudal regions of the hippocampus were embedded and flash frozen in Tissue-Plus™ O.C.T. compound (Thermo Fisher Scientific). Tissue blocks were cryosectioned into 10-µm thick coronal sections and stored at −80 °C until further processed. Each slide contained two groups of consecutive brain sections where each group contained two sections from different locations of the hippocampus.

All brain sections processed for a specific biomarker were immunostained at the same time using the same batch of reagents to ensure comparable experimental conditions across all samples. Slides were brought to RT and then dried at 50 ^{o}C for 15 min. Brain sections were permeabilized with 0.5% (v/v) Triton X-100 (Thermo Fisher Scientific) in PBS for 5 min and subsequently washed in PBS. Slides were placed in 10 mM sodium citrate buffer (Thermo Fisher) at pH 6.0 and heated for 30 min in a vegetable steamer (Black & Decker, Flavor Scenter Steamer) for antigen retrieval (89 $\pm$ 1 ^{o}C final temperature). Following antigen retrieval, slides were segmented into two hydrophobic wells with a PAP pen (Sigma-Aldrich, St. Louis, MO), with each well containing two sections of the CA1 hippocampus. Sections were incubated in blocking buffer containing 10% (v/v) normal goat serum (Vector Laboratories, Burlingame, CA, USA), 1% (w/v) bovine serum albumin (Sigma-Aldrich), and 0.03% (v/v) Triton X-100 (Thermo Fisher Scientific) in PBS for 1 h at RT. Next, sections were incubated with guinea pig anti-MAP2, mouse anti-PSD95 (validated in Supplementary Fig. S1), rabbit anti-SV2A (validated in Supplementary Fig. S2-S4) primary antibodies (Table 1) in blocking buffer at 4 °C overnight. Sections were washed with 0.03% (v/v) Triton X-100 in PBS and then incubated with goat anti-guinea pig, goat anti-mouse, and goat anti-rabbit secondary antibodies (Table 2) in blocking buffer for 2 h at RT. Sections were washed in PBS, then treated with TrueBlack® Lipofuscin Autofluorescence Quencher (Biotium, Fremont, CA), and mounted in ProLong™ Gold Antifade Mountant with DAPI (Invitrogen, Thermo Fisher Scientific, Waltham, MA). As a negative control, sections from each time point were incubated with blocking buffer rather than primary antibody, but otherwise processed identically (Supplementary Fig. S5).

Table 1: List of primary antibodies used for immunohistochemistry (IHC) and western blotting (WB)

1° Antibody	Host	Source	Location	Product #	Lot #	Dilution	Clonality	Clone	Subclass	RRID
Anti-SV2A	Rabbit	Abcam	Waltham, MA, USA	ab254351	GR3346152-1	1:100 IHC 1:1000 WB	Mono	EPR23500-32	IgG	AB_2885082
Anti-rabbit IgG	Rabbit	Abcam	Waltham, MA, USA	ab172730	GR3235749-22	1:100	Mono	EPR25A	IgG	AB_2687931
Anti-PSD95	Mouse	Thermo Fisher	Waltham, MA, USA	MA1-046	VJ307784	1:100 IHC 1:1000 WB	Mono	7E3-1B8	IgG1	AB_2092361
Anti-MAP2	Guinea Pig	Synaptic Systems	Göttingen, Germany	SySy 188004	3-33	1:500	Poly	N/A	N/A	AB_2138181
Anti-β Actin	Mouse	Licor	Lincoln, NE, USA	926-42212	D01217-01	1:1000	Mono	N/A	IgG 2b	AB_2756372

Table 2: List of secondary antibodies used for immunohistochemistry and western blotting

2° Antibody	Host	Reactivity	Source	Product #	Lot #	Dilution	Fluorophore	Antibody used with	RRID
Anti-rabbit IgG (H+L) highly cross-absorbed	Goat	Rabbit	Invitrogen	A11036	2155282	1:1000	AlexaFluor 568	SV2A & rabbit IgG	AB_10563566
Anti-mouse IgG1 highly cross-absorbed	Goat	Mouse	Invitrogen	A21240	2185066	1:1000	AlexaFluor 647	PSD95	AB_2535809
Anti-guinea pig IgG (H+L) highly cross-adsorbed	Goat	Guinea Pig	Invitrogen	A11073	982288	1:1000	AlexaFluor 488	MAP2	AB_2534117
Anti-rabbit IgG	Goat	Rabbit	Licor	926-68071	D01209	1:10,000	IRDye 680CW	SV2A	AB_10956166
Anti-mouse IgG	Goat	Mouse	Licor	926-32210	C80816-15	1:10,000	IRDye 800CW	PSD95 & β Actin	AB_621842

4.2: Fluorescent Image Acquisition

Fluorescent image stacks were acquired with an IX-81 inverted microscope and MetaMorph Image Analysis Software using a 60X objective lens (Olympus UPLANFLN 60x/1.25na Oil Iris). Sections were wide-field illuminated with a Lumencor SOLA light engine to stimulate the fluorescence of AlexaFluor® conjugated secondary antibodies and DAPI. Light was filtered through DAPI, FITC, mCherry, and CY5 optical filters corresponding to DAPI, AlexaFluor 488, 568, and 647 nm antibodies, respectively. Image stacks of two brain sections from each well were captured for up to four sections imaged per animal. Additionally, from each brain section image stacks were acquired of the *stratum oriens* (S.O.), *stratum pyramidale* (S.P.), and *stratum radiatum* (S.R.) layers of the CA1, selected by an individual blinded to group. Regions of interest (ROIs) were randomly selected using the DAPI channel from roughly the same neuronal clusters (no overlap) from each layer of the CA1. The other channels were screened while

setting the z-series parameters to ensure good image quality before capturing. Each plane of the series was exposed for 1000 ms at 10% light engine intensity and detected by a CCD camera with maximum image size of 1392 x 1040 pixels. A total z-distance of 6-µm with a 0.2-µm z-step was captured for each series of images, corresponding to voxel dimensions of 0.1075 x 0.1075 x 0.2 µm in x, y, and z directions.

4.3: Image Stack Deconvolution

All image stacks were deconvolved with Huygens Professional software (Scientific Volume Imaging, Hilversum, Netherlands) using a wide-field deconvolution license.

The general parameters were as follows: Microscopic parameters: X, Y, and Z sampling intervals were 108, 108, and 200 nm, respectively. Optical parameters: The objective numerical aperture (na) was 1.250, and the lens immersion oil and Permount Mounting Medium na were 1.518. Advanced parameters: good objective quality, coverslip position of 0.00 µm, and a downward imaging direction. Channel parameters: A wide-field microscope type with the following channels: Alexa Fluor 568 (channel 0; excitation λ578, emission λ603), Alexa Fluor 647 (channel 1; excitation λ650, emission λ665), Alexa Fluor 488 (channel 2; excitation λ490, emission λ525), DAPI (channel 3; excitation λ350, emission λ470). For all channels, the multiphoton excitation was set to 1 and the excitation fill factor was set to 2.

Batch deconvolution was performed on all images with a custom workflow that selected the image series, set the microscopic parameters, stabilized z-slices, performed deconvolution, and set the location to save the images. For each image the deconvolution wizard parameters were as follows: For each channel, a theoretical point spread function (PSF) was calculated, the background was automatically estimated, and a classic maximum likelihood estimation (CMLE) algorithm was applied. The CMLE parameters included a maximum of 50 iterations, a signal to noise ratio of 20, a quality threshold of 0.05, iteration mode set to “optimized,” and the brick layout set to “auto.” All deconvolved image stacks were saved in the “Imaris Classic” file format and subsequently batch converted to IMS 5.5 format.

4.4: Image 3D Reconstruction and Quantitative Analysis

4.4.1: Imaris Segmentation

IMS 5.5 image files were imported into Imaris version 9.7 (Bitplane, Zurich, Switzerland). The MAP2 channel was used to create a 3D rendering of the dendritic branches and cell bodies using "Surfaces," and the PSD95 and SV2A puncta were 3D reconstructed using "Spots." Due to imaging limitations, only puncta larger than 3 voxels (0.00693 μm^3) were counted. PSD95 and SV2A puncta were digitally associated with dendrites if Spots were within the range of 0.5 μm below or 1.0 μm away from the MAP2 Surfaces. Spots outside this range were considered non-synaptic. Additionally, PSD95 and SV2A puncta were digitally associated if Spots were within 0.5 μm from one another. Classification filters were applied to the Spots to define excitatory and inhibitory synapses, the colocalization of PSD95 and SV2A Spots, and non-synaptic SV2A puncta. The full analysis algorithm can be found in the supplementary file (Supplementary Section 3).

4.4.2: Biomarker Quantification

MAP2 immunoreactivity was quantified using the Surface volume that was normalized to volume of the region. Synaptic immunoreactivity was quantified using the Spot classifications and all the following metrics were normalized to the volume of MAP2 Surfaces. Excitatory synapses were defined as the PSD95 and SV2A spots that were digitally associated with each other and MAP2 Surfaces. Inhibitory synapses were indirectly assessed, and they were defined as SV2A Spots associated with MAP2 Surfaces but not associated with PSD95 Spots. The colocalization of PSD95 and SV2A puncta was defined as the percentage of SV2A spots that were digitally associated with PSD95 Spots and MAP2 Surfaces. Non-synaptic SV2A was defined as the percentage of SV2A Spots that were not associated with PSD95 Spots or MAP2 Surfaces.

5. *In vivo* Imaging

5.1: SV2A PET Radiotracer Synthesis

The SV2A radiotracer ([^{18}F]-SDM-8) was obtained from the University of California Davis Center for Molecular and Genomic Imaging (CMGI). The synthesis of [^{18}F] SDM-8 was performed according to an established method [36].

5.2: *In vivo* imaging and analysis

5.2.1: Animals

Imaging studies were performed at the CMGI at 10 and 28 days post-exposure (DPE). Immediately prior to imaging, animals were anesthetized with isoflurane/O2 (Piramal Healthcare, Bethlehem PA) using 2.0-3.0% vol/vol to induce anesthesia and 1.0-2.0% vol/vol to maintain anesthesia. Anesthetized animals were placed in a stereotaxic head holder and imaged for up to 60 min for PET and 30 min for MRI. Throughout imaging, the animal's body temperature was maintained at 37°C using warm air or a heat lamp, and anesthesia was adjusted to maintain a respiration rate of 50-70 breaths per min.

5.2.2: Magnetic resonance imaging (MRI)

MRI scans were performed using a Bruker Biospec 70/30 (7T) preclinical MR scanner (Bruker BioSpin MRI GmbH, Ettlingen, Germany) equipped with a 116 mm internal diameter B-GA12S gradient (450 mT/m, 4,500 T/m/s), a 72-mm internal diameter linear transmit coil, and a 20 mm internal diameter surface coil for signal reception. Scans consisted of a 2-D, multislice, T2-weighted (T2w), RARE protocol covering the whole brain (approximately 12.0 to -17.5 mm Bregma) acquired using Paravision 6.1 (Bruker BioSpin MRI GmbH) with the following parameters: repetition time (TR) = 6250 ms; echo time (TE) = 33 ms; RARE factor = 8; averages = 4; field of view (FOV) = 35 × 25 × 29.5 mm^3, and in-plane data matrix of 280 × 200 × 59. The resolution of reconstructed images for all scans was 0.125 × 0.125 × 0.5

mm^3.

The hippocampus (approximately -2.0 to 6.5 mm Bregma) was manually delineated on sequential, axial, images based on Paxinos and Watson's The Rat Brain in Stereotaxic Coordinates (Paxinos and Watson 2007) using AMIRA 6.1 (Thermo Fisher Scientific, Waltham, MA). A cerebral reference region consisting of a 1.5 x 1.0 x 1.5 mm ellipsoid centered on 11.5 mm bregma was placed using PMOD v4.2 (PMOD Technologies, Zurich, CHE).

5.2.3: Positron emission tomography (PET)

PET scans were performed using one of two preclinical PET systems (Inveon Dedicated PET; or microPET Focus 120; both Siemens Medical Solutions, Knoxville, TN). Each animal was imaged on the same scanner when across time points. Anesthetized animals received a tail-vein injection of PET radiotracer (~37 MBq in 200 µl saline) at the initiation of a 60-minute scan. PET data were reconstructed into seven frames (time intervals included: 0-10, 0-20, 10-30, 20-40, 30-50, 40-60, and 50-60 minutes) using two iterations of the 3-D ordered subset expectation maximization (OSEM3D) method followed by 18 iterations of a maximum a posteriori (MAP) algorithm. The imaging matrix was 128 × 128 × (95 or 159; scanner dependent) with reconstructed voxel sizes of 0.86 mm × 0.86 mm × 0.80 mm. PET images were co-registered to T2w MRI using PMOD v4.2 (PMOD Technologies, Zurich, CHE). VOIs delineated on T2w scans were used from regional analysis of PET images. For each VOI the mean standardized uptake value (SUV) and SUV normalized to the cerebellar VOI (SUV ratio, SUVR) were calculated over each reconstructed frame.

6. Statistics

6.1: Dendritic Arborization Analyses

A Mixed Model structure was used to fit data from the Sholl, AUC, and non-Sholl neuronal metrics using

SAS JMP® Pro version 15. A separate model was used for the Sholl analysis that held Group as a fixed effect and the Sholl radius nested within Neuron ID as a random effect. The model also used a Repeated Covariance Structure with a first-order autoregression (AR(1)) structure that used a repeated ID (animal, neuron ID, radius) and held animal as the subject. The Sholl AUC and non-Sholl derived neuronal metrics were fit to a model that held exposure as a fixed effect and used a Residual structure for the Repeated Covariance Structure.

6.2: Dendritic Spine Density and Morphology Analyses

Due to differences in dendritic segments studied on the two post-exposure days, analyses were conducted separately for each day. To account for the repeated measures within an animal (across neurons and dendrites), mixed effects models were used to estimate the difference between the DFP and VEH groups. These models further included an animal-specific random intercept to account for the correlation among observations from the same animal.

6.3: Quantitative Immunohistochemical Analyses

Key outcomes include MAP2 immunoreactivity, excitatory synapses, inhibitory synapses, percentage of colocalized puncta, and percentage of non-synaptic SV2A. The first set of analyses utilized measurements at the region (dorsal or ventral) and layer (S.O., S.P., and S.R.) level for each animal. Mixed effects models were used to assess differences by exposure group (VEH or DFP), region, layer, and days post-exposure (10 or 28 DPE). Interactions between the factors (exposure, region, layer, and day) were considered, and the best model was chosen using Akaike Information Criterion. Excitatory synapses, inhibitory synapses, percentage of non-synaptic SV2A data were transformed using the natural logarithm to better meet the assumptions of the model. Contrasts for group differences were constructed and tested using a Wald test. The Benjamini-Hochberg false discovery rate (FDR) was used within an outcome measure to account for multiple comparisons. Results are presented as geometric

mean ratios (GMR) between exposure groups for the log-transformed outcomes and as differences between exposures for excitatory synapses, inhibitory synapses, and percentage of non-synaptic SV2A. Point estimates of the ratios or differences and 95% confidence intervals are presented in the figures. When the confidence interval for the GMR includes 1, there is no statistical evidence of a difference between groups; similarly, when the confidence interval for the differences includes 0, there is no statistical evidence of a difference between groups.

A second set of analyses averaged across regions and layers for each outcome so that each animal had only a single observation for each outcome. Linear regression was used to assess group differences. The only factors of interest in these models were group and day; the interaction was also considered. As for the mixed effects models, Akaike Information Criterion was used to select the best model for each outcome. GMR or mean differences are reported. All analyses were performed using SAS software, version 9.4 and alpha was set at 0.05; all reported results remained significant after the FDR procedure.

6.4: *In Vivo* Imaging Analyses

Analysis of PET data was performed in GraphPad Prism v9.2. SUV calculated from a range of time frames during PET data acquisition were compared across two groups (DFP and vehicle) and at two time points (10- and 28-days) using a three-way ANOVA. Correction for multiple comparison was performed using the Benjamini, Krieger and Yekutieli two-stage step-up method for calculating the false detection rate (FDR). FDR corrected p-values < 0.05 were considered significant. The SUVs derived from PET data were correlated to dendritic spine density and synaptic IHC using Spearman correlation. Correlations with histological metrics utilized the final imaging time point of all DFP-exposed and VEH animals.

Results:

Acute DFP intoxication triggered *status epilepticus (SE)* in adult male rats

To confirm the DFP exposure paradigm used in these studies (Fig. 1A) triggered SE, DFP-intoxicated rats were monitored for seizure behavior as previously described [30], and all animals (n = 28/28) exhibited characteristic signs of cholinergic crisis (i.e., SLUD: salivation, lacrimation, urination, defecation) within minutes after intoxication. However, only DFP exposed rats that achieved a maximal seizure score of $\geq$ 3 and an average seizure score of 2.5 over the first 240 min (Fig. 1B, C) were included in this study (n = 27/28).

Acute DFP intoxication increased basilar dendritic arborization of pyramidal neurons and decreased MAP2 IR in the CA1 hippocampus

Golgi-stained pyramidal neurons were analyzed in the CA1 hippocampus at 10 and 28 DPE (Fig. 2A, B). At 10 DPE, DFP intoxicated animals displayed increased distal (70-280 μm) arbor complexity ($p = 0.0154$) compared to VEH animals as determined from Sholl plots (Fig. 2C). Significantly increased total dendritic length ($p = 0.0340$) and dendritic complexity ($p = 0.0319$) were also observed in 10 DPE DFP animals, while cell body area was not significantly different between DFP and VEH groups at either time post exposure (Fig. 2D). No significant group differences were measured in 28 DPE animals or other measures of dendritic arbor complexity (Supplementary Fig. S6).

Dendrite effects of acute DFP intoxication were further assessed by quantifying immunoreactivity (IR) for MAP2, a dendrite selective biomarker, in the S.O. (top), S.P. (mid), and S.R. (bottom) layers of the CA1 hippocampus (Fig 3A) across rostral, medial, and caudal hippocampal slices. Overall, DFP animals had significantly lower MAP2 IR than VEH animals with no interaction between group and DPE (10 and 28; mean difference = -0.03; 95% CI = (-0.04, -0.01); $p < 0.001$; Fig. 3 left). When considering all CA1

layers and anatomical locations, MAP2 IR varied by anatomical location and DPE, with significantly decreased MAP2 IR in DFP animals at 10 DPE in the medial (mean difference = -0.08; 95% CI = (-0.12, -0.04); $p < 0.001$) and caudal (mean difference = -0.03; 95% CI = (-0.04, -0.01); $p < 0.001$) locations of the hippocampus compared to the VEH group (Fig. 3 right). Additionally, we observed increased numbers of DAPI-positive nuclei in the CA1 hippocampus at 10 ($p < 0.0001$) and 28 DPE ($p = 0.0115$) in DFP exposed animals (Supplementary Fig. S7).

Acute DFP intoxication did not significantly alter dendritic spine density or synaptic biomarkers at delayed times post-exposure

Dendritic spines are the site of the majority of excitatory synapses in the CNS and are strongly implicated in mechanisms of learning and memory [37]. To determine whether acute DFP intoxication altered the density of excitatory synapses in the CA1, dendritic spines were characterized on dendritic segments of Golgi-stained pyramidal neurons 50–75 µm from the cell body in 10 DPE animals and 75-100 µm in 28 DPE animals (Fig. 4A). There were no significant differences in dendritic spine density between the DFP and VEH animals at 10 DPE (mean difference = 0.04, 95% CI = (-0.04, 0.12), $p = 0.3$) or 28 DPE (mean difference = -0.06, 95% CI = (-0.19, 0.07), $p = 0.34$; Fig. 4B, C). Next, using length and width measurements, dendritic spines were characterized according to morphological subtypes commonly found on pyramidal neurons: filopodia, long thin, thin, stubby, and mushroom, which represent less to more mature spine phenotypes (Fig. 4D). We observed a significantly increased percentage of protrusions classified as filopodia in DFP relative to VEH animals at 10 and 28 DPE ($p = 0.04$). Additionally, at 10 DPE, DFP animals also displayed significantly decreased percentages of long thin ($p = 0.01$) and thin spines ($p = 0.001$), whereas they had a significantly increases percentage of mushroom spines ($p < 0.001$).

Quantitative immunohistochemistry, using antibodies against presynaptic SV2A, postsynaptic PSD95, and dendritic MAP2, was used to measure excitatory and inhibitory synapses at 10 and 28 DPE (Fig. 5). Excitatory synapses were defined as puncta co-labeled for PSD95 and SV2A that were associated with MAP2-positive processes. Overall, excitatory synapses were not significantly different between DFP and VEH animals (Fig. 5B left). However, when considering all observations (Location, Layer, and DPE), the best model suggested that differences between DFP and VEH animals varied by CA1 layer, but not by hippocampal region or DPE. In this model, excitatory synapses were significantly increased in the S.P. layer (GMR = 1.58; 95% CI = (1.12, 2.23); p = 0.01; Fig. 5B right). Inhibitory synapses were defined as SV2A immunoreactive puncta associated with MAP2-positive volume that were not immunoreactive for PSD95. Inhibitory synapses were not significantly different between DFP and VEH animals (Fig 5C left). When considering all observations, the best model suggested differences between DFP and VEH varied by hippocampal location, with the main difference in the rostral region (GMR = 1.40; 95%CI = (1.01, 1.95); p = 0.04); however, this did not remain significant after FDR (Fig. 5C right). Tables containing breakdowns of the IHC statistics (ratios, 95% CIs, and p-values) by measurement, DPE, location, or layer (Supplementary Section 6) and additional spatial localization of SV2A IR data (Supplementary Fig. S8) can be found in the supplementary file.

Inspection of the PET SUV images revealed minimal off-target uptake outside the brain and relatively homogenous radiotracer uptake across cortical and midbrain structures. SUV analysis is an ongoing area of development in the field of SV2A PET imaging [38, 39], therefore SUVs were calculated from data collected during a range of time windows during PET scanning (10-30, 20-40, 30-50 and 40-60 min). Regional analysis of average SUV within the hippocampus indicated a trend towards radiotracer uptake in DFP intoxicated animals, particularly at the 28-day time point; however, no significant differences were detected between DFP and vehicle groups at either 10 or 28 DPE, regardless of SUV framing (Fig. 6B).

Positive correlations between Golgi and SV2A PET synaptic density metrics, but not IHC metrics were identified in the rat model of acute DFP intoxication

We performed Spearman correlation analyses of the PET SUV and histological assessments of synaptic density from animals that received *in vivo* and *ex vivo* measurements at 28 DPE. The early framing interval (from 10-30 mins post radiotracer injection) displayed a positive correlation between SUV and dendritic spine density ($r = 0.631$; 95% CI = (0.134, 0.874); $p = 0.0181$; Fig. 6C). Correlations from later SUV framing intervals became progressively less significant; 20-40 mins frame ($r = 0.552$; 95% CI = (0.0123, 0.842); $p = 0.0438$) and at the 30-50 mins frame no significance was detected ($r = 0.499$; 95% CI = (-0.0605, 0.82); $p = 0.0721$). Additionally, correlations between dendritic spine density and the right anterior hippocampal SUV, where histological observations were measured, displayed a stronger correlation than when compared to the whole hippocampal SUV ($r = 0.631$ and $r = 0.547$, respectively). However, there were no significant correlations between PET SUV and synaptic IHC metrics.

Figures and Legends:

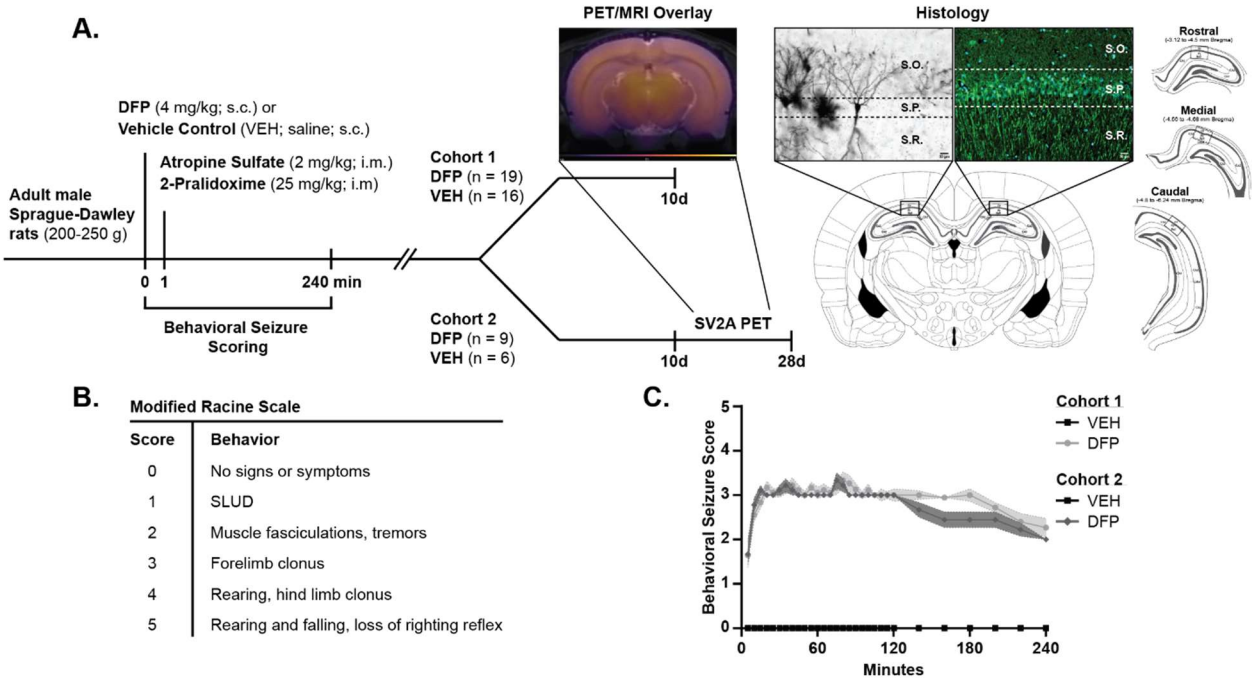

Fig. 1: Schematic representation of the DFP exposure paradigm and experimental timeline. **A.** Two independent cohorts of adult male Sprague-Dawley rats were administered a single dose of DFP or VEH followed 1 min later by atropine sulfate and 2-pralidoxime. Rats were monitored for seizure behavior up to 240 min post-exposure. Rats in Cohort 2 underwent *in vivo* imaging (MRI & PET) at 10 and 28 days post-exposure (DPE). Within 24 h of the last *in vivo* imaging session, rats were euthanized to collect brain tissue for histological analyses. The left hemispheres were processed for Golgi staining; the right, for immunohistochemistry (IHC). Golgi-stained pyramidal neurons in the CA1 hippocampus were selected for morphometric analysis from the *stratum oriens* (S.O.) and *stratum pyramidale* (S.P.) layers, while morphometric analysis of immunostained neurons focused on neurons in the S.O., S.P., and *stratum radiatum* (S.R.) at 3 distinct anatomical locations (rostral, medial, and caudal). **B.** A modified Racine scale was used to score seizure behavior at 5–min intervals from 0 to 120 min post-DFP and at 20-min intervals from 120 to 240 min post-DFP. **C.** The average seizure score, calculated as the time-weighted average of the animal's individual seizure scores across the 4 h of observation (Cohort 1: VEH

n=16, DFP n=18; Cohort 2; VEH n=6, DFP n=9). Data presented as the mean ± S.E.M. SLUD = salivation, lacrimation, urination, defecation.

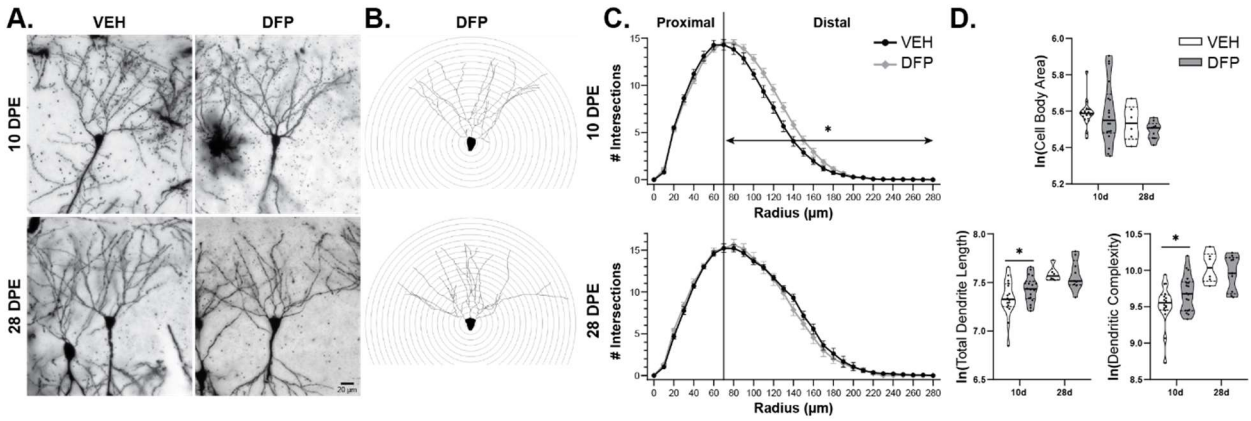

Fig. 2: Acute DFP intoxication increased arborization of the basilar dendrites of Golgi-stained CA1 pyramidal neurons at 10 days post-exposure (DPE). Data presented is for VEH and DFP groups at 10 DPE (VEH n=16, DFP n=18) and 28 DPE (VEH n=6, DFP n=9). **A.** Representative photomicrographs and **B.** Neurolucida reconstructions of basilar dendrites of Golgi stained neurons. Reconstructed images are of neurons from the DFP animals. **C.** Sholl plots from 10 DPE (top) and 28 (bottom) DPE. Values indicate the group's mean number of intersections at each Sholl radius (± S.E.M.). Mixed effects models were used to identify group differences in the area under the curve (AUC) for the total (0-280 μm), proximal (0-70 μm), and distal (70-280 μm) portions of the Sholl plots. At 10 DPE, the average distal AUC was significantly increased ($p = 0.0154$) in DFP animals relative to VEH controls. **D.** Violin plots represent the median and quartile values of the cell body area, total dendritic length, and dendritic complexity, with each dot representing an individual animal. At 10 DPE, the natural logarithm of dendritic complexity ($p = 0.0319$) and the total dendrite length ($p = 0.0340$) in DFP animals were significantly increased relative to VEH controls. * $p < 0.05$. Dendritic complexity = [# nodes + # endings] * [total dendritic length/# dendrites].

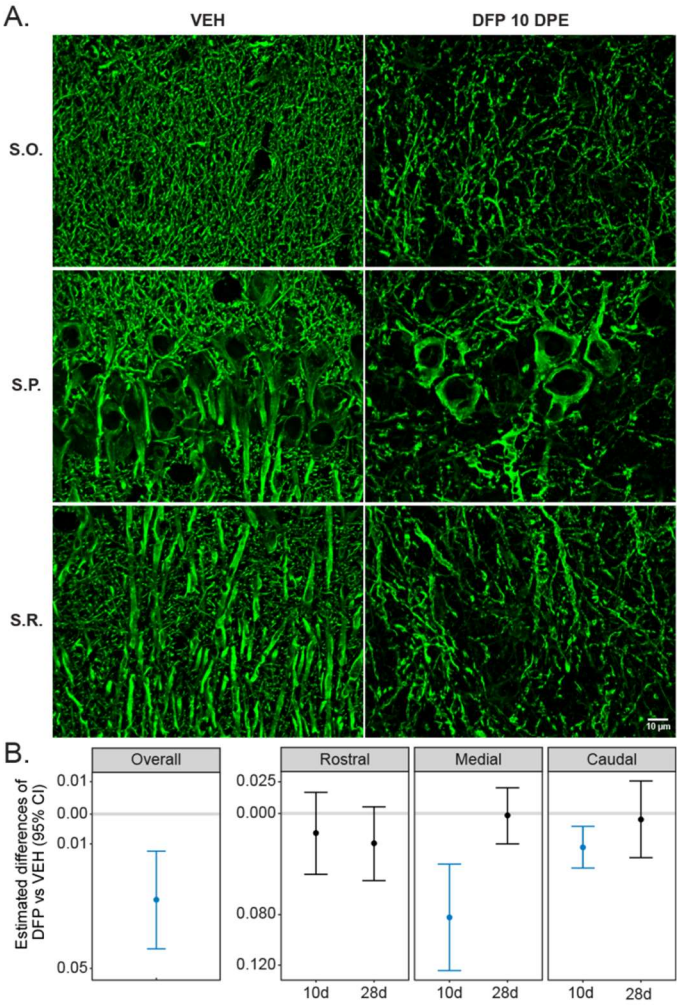

Fig. 3: Acute DFP intoxication significantly decreased MAP2 immunoreactivity (IR) in the CA1 hippocampus. **A.** Representative photomicrographs of MAP2 IR (green) in the *stratum oriens* (S.O.), *stratum pyramidale* (S.P.), and *stratum radiatum* (S.R.) layers of VEH and DFP animals at 10 days post-exposure (DPE). **B.** There was no significant interaction between DPE and experimental group, and the estimated mean difference for MAP2 IR was significantly lower in DFP than in VEH animals (Overall: $p < 0.001$). The estimated mean differences between VEH and DFP groups varied by hippocampal location (rostral, medial, or caudal) and DPE, with the DFP group having significantly lower levels of MAP2 IR than the VEH group in the medial ($p < 0.001$) and ventral ($p = 0.002$) regions at 10 DPE. An estimated mean difference with a 95% confidence interval (CI) that crosses the 0.00 intercept indicates no significant difference between groups. An estimated mean difference with a 95% CI above or below the 0.00

intercept indicates a significant increase or decrease, respectively. Blue CIs identify significant differences between DFP and VEH groups ($p < 0.05$). All data presented are for VEH and DFP groups at 10 (VEH n=15, DFP n=17) and 28 DPE (VEH n=6, DFP n=9).

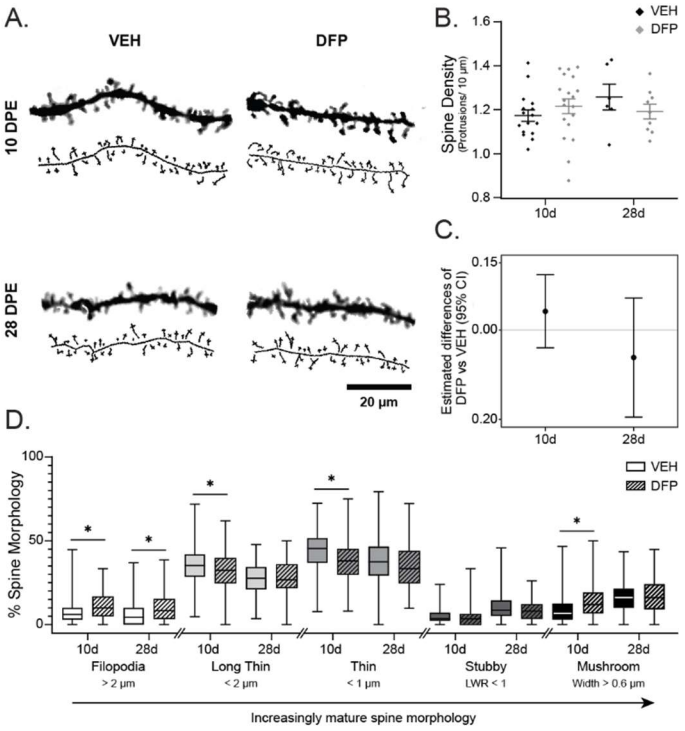

Fig. 4: Acute DFP intoxication did not significantly alter dendritic spine density in the CA1, but significantly increased the percentage of spines with immature morphology at 10 (VEH n=16, DFP n=18) and 28 VEH n=6, DFP n=9) days post-exposure (DPE). **A.** Representative photomicrographs of dendritic spines of Golgi-stained neurons and their reconstructed spine profiles. Spine density at 10 DPE was measured on dendritic segments located 50 – 75 µm from the cell body; at 28 DPE, on dendritic segments 75-100 µm from the soma. **B.** The mean spine density for each animal was calculated from the average spine density of five neurons across two to three dendritic segments per neuron. The data are presented as the mean (± S.E.M) spine density per 10 µm of dendritic length. **C.** The estimated difference between DFP and VEH was not significantly different from 0.00 at either DPE, as indicated by the fact that the 95% confidence interval (CI) included the 0.00 intercept. **D.** Dendritic spines were

characterized in order of spine maturity (left to right) based on spine morphology. Group data are presented as box plots representing the median and 25-75 percentile and whiskers indicating minimum and maximum values. The percent of spines classified as filopodia was significantly higher in DFP than VEH animals at 10 and 28 DPE ($p = 0.04$). * $p < 0.05$

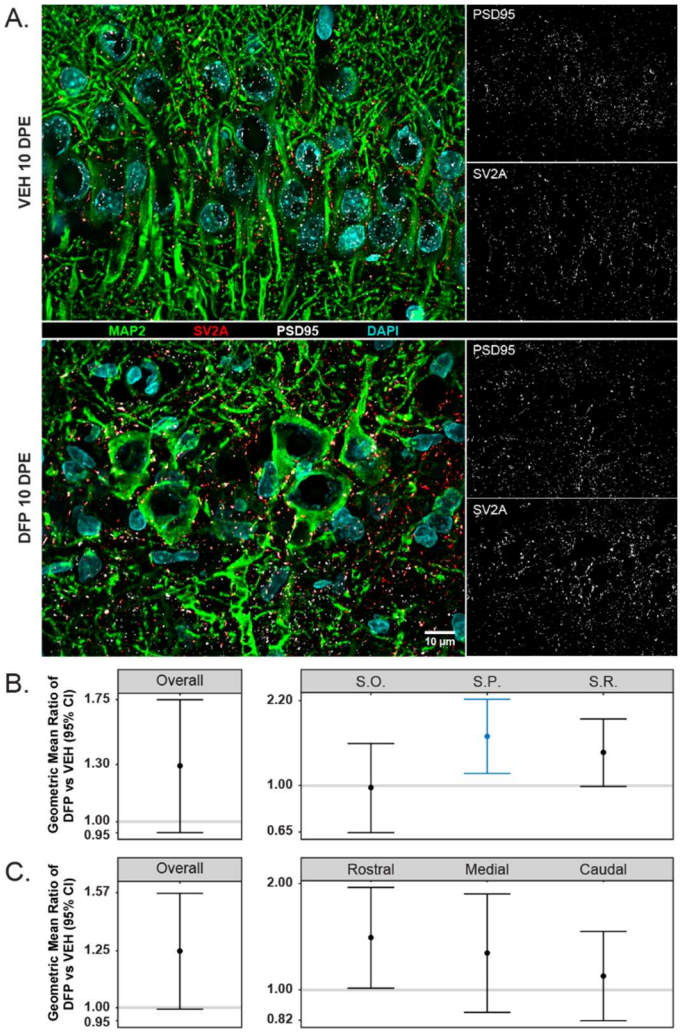

Fig. 5: Acute DFP intoxication significantly increased excitatory synapses in the *stratum pyramidale* (S.P.) layer of the CA1 but did not significantly alter synaptic density overall at 10 or 28 DPE. All data presented are for VEH and DFP groups at 10 (VEH n=15, DFP n=17) and 28 DPE (VEH n=6, DFP n=9). **A.** Representative photomicrographs of the S.P. layer from VEH (top) and DFP (bottom) groups. Large panels correspond to a composite of MAP2 (green), PSD95 (white), and SV2A (red) immunoreactivity

(IR), counterstained with DAPI (cyan); small panels show the individual stains. **B.** Excitatory synapses were defined as puncta co-labeled by PSD95 and SV2A that were associated with MAP2-positive dendrites. The geometric mean ratio (GMR) of the number of excitatory synapses in the CA1 of DFP *vs*. VEH was not significantly different when averaged across all layers (overall). However, the number of excitatory synapses was significantly increased in DFP animals relative to VEH in the *stratum pyramidale* (S.P.) layer ($p = 0.01$). **C.** Inhibitory synapses were defined as the SV2A immunoreactive puncta associated with MAP2-positive dendrites that did not co-localize with PSD95 IR. There was no significant difference between DFP and VEH in the number of inhibitory puncta overall or in any layer of the CA1 hippocampus. A GMR with a 95% CI that crosses the 1.0 intercept indicates no significant difference. A GMR with a 95% CI above or below the 1.0 intercept indicates a significant increase or decrease, respectively. Blue CIs indicate a significant difference between DFP and VEH ($p < 0.05$).

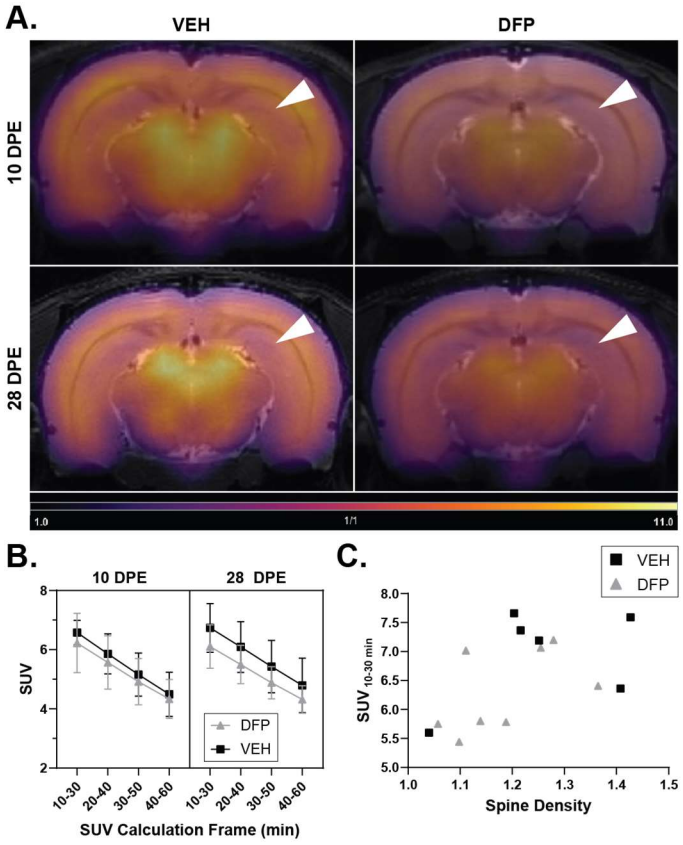

Fig. 6: Acute DFP did not significantly alter hippocampal synaptic density measured by SV2A PET at 10 or 28 DPE; however, PET SUV at 28 DPE is positively correlated with dendritic spine density as determine by histology. **A.** Representative parametric images of SV2A PET SUV registered on T2-weighted (T2w) MRIs from VEH and DFP groups acquired longitudinally at 10 (VEH n=4, DFP n=6) and 28 (VEH n=6, DFP n=8) days post-exposure (DPE). Volumes of interest (VOI) delineated on T2w scans were used for dorsal anterior (white arrow) and whole hippocampal analysis of PET images. **B.** Line graphs depicting PET radiotracer uptake in DFP vs. VEH control animals at 10 and 28 DPE assessed by standard uptake values (SUV) calculated across a range of time windows during PET data acquisition (Fig. 6B). No significant differences were observed between DFP and VEH at either time point (all comparisons $p>0.05$), although there is a trend towards reduced SV2A labeling by the radiotracer in the DFP animals at both time points. Note, the x-axis indicates the range of time windows post injection of radiotracer utilized

for quantifying radiotracer uptake (SUV), and the relationship between DFP and vehicle exposure remains constant regardless of the time window used to calculate SUV. Data presented as mean (± SD). **C.** Scatter plot depicting the relationship between PET SUV from the 10-30 min frame and dendritic spine density in 28 DPE animals. The Spearman's correlation coefficient was r = 0.631; 95% CI = (0.134, 0.874); p = 0.0181.

Discussion:

Previous studies have reported dendritic and synaptic damage in the hippocampus within hours of acute OP intoxication [22-24]; however, it is unknown whether these effects persist at more delayed times post-exposure. In the present study, we assessed the effects of acute DFP intoxication on the cytoarchitecture of dendrites and synapses at 10 and 28 DPE. We observed increased dendritic complexity at the level of individual neurons but decreased regional MAP2 IR that varied with time. Although we did not observe altered synaptic density at later times post-exposure, because dendritic morphology is a critical determinant of synaptic connectivity [40-42], our findings support the hypothesis that altered synaptic connectivity, may contribute to the pathogenesis of chronic morbidity associated with acute OP intoxication. Finally, we observed positive correlations between *in vivo* and *ex vivo* methods of quantifying synaptic density that support our histological finding and suggest SV2A PET could be evaluated further as a tool for assessing synaptic effects of acute OP intoxication.

Significant dendritic regression in the hippocampus has been reported within one hour after acute DFP exposure, an effect that was attributed to anticholinesterase-induced neuronal hyperactivity [23]. In contrast, using Golgi staining, we observed increased dendritic length and complexity of individual pyramidal neurons in the hippocampus at 10 DPE from morphometric analyses. Conversely, regional MAP2 IR was decreased in the hippocampus of DFP animals. Since acute DFP intoxication has been shown to cause significant neuronal cell death in the hippocampus during the days and weeks

post-exposure [30, 43], one interpretation of these seemingly discrepant observations is that the dendritic arborization of surviving neurons is a compensatory mechanism for maintaining network balance. A similar phenomenon has been observed in animal models of SE triggered by factors other than OPs [44-46]. The enhanced dendritic growth of individual neurons does not appear to be a non-specific effect of general cellular hypertrophy since the cell body area of Golgi-stained neurons was not significantly different between DFP and VEH. Interestingly, by 28 DPE, there were no significant differences in dendritic complexity between DFP and VEH. Therefore, the dendritic effects of acute OP intoxication seem to be biphasic, marked by early atrophy of dendritic arborization [24] followed by a transitory overgrowth that subsides back to "baseline" levels by one month post-exposure.

Dendritic damage evidenced as decreased MAP2 IR in the CA1 hippocampus has been demonstrated in other rat models of seizures [12, 14]. For example, pilocarpine-induced SE decreased MAP2 IR in the CA1 at 14 days post-exposure, and despite modest recovery, remained decreased at 35 days post-SE. In the rat DFP model, MAP2 IR was more severely decreased in DFP animals at 10 DPE than at 28 DPE but remained decreased relative to VEH at 28 DPE. Furthermore, consistent with our previous studies that DFP-induced SE triggered a robust neuroinflammatory response [8, 10, 11], we observed increased numbers of nuclei in the CA1 that coincided with the decreased MAP2 IR (Supplementary Fig. S7). Increased nuclei number was also observed in the rat CA1 after pilocarpine-induced SE and shown to reflect increased numbers of microglia that spatiotemporally coincided with decreased MAP2 IR [12, 14]. Interestingly, many of the cytokines known to be released by microglia, have been shown to influence dendritic arborization (ref).

Previous studies of synaptic connectivity at one hour after acute intoxication with DFP demonstrated spatiotemporal coincidence of dendritic regression and decreased synaptic density and expression of synaptic proteins [22-24]. Using quantitative IHC and SV2A PET, we observed subtle but

significant changes in synaptic connectivity that were regionally and time-dependent. Specifically, we observed increased SV2A IR in the S.P. layer of the CA1, which drove the significant increase in excitatory synapses observed in DFP animals at 10 DPE. This observation is consistent with what was reported 10 days after pilocarpine-induced SE [47]. However, when the observations from CA1 layers and anatomical locations were averaged to assess animal level effects, no differences were detected between DFP and VEH animals. Similarly, no significant differences in uptake of the SV2A PET radiotracer were measured in these animals at 10 or 28 DPE, although the SUV group means trended lower in DFP relative to VEH at both 10 and 28 DPE. However, our analysis of spine morphology suggests that synaptic plasticity may be altered at delayed times after acute DFP intoxication. Specifically, at 10 DPE, relative to VEH controls, DFP hippocampal neurons exhibited significant increases in the percentage of spines with the most immature morphology (filopodia) and the most stable, mature spine type (mushroom) but significant decreases in the percentages of long and thin morphologies. This is consistent with previous reports that dendritic spine morphology is modulated in response to excitotoxic stimuli, such as seizures [48]. Dendritic spines comprise the majority of excitatory synaptic sites, and changes in density or morphology of these structures are strongly implicated in mechanisms of synaptic plasticity, learning, and memory [37, 49, 50].

Histological assessments are widely used to measure local changes in synaptic density in brain slices; however, SV2A PET has recently been employed for global, longitudinal measurements of synaptic density in the intact living brain. Decreased SV2A as assessed by PET imaging has been associated with many of the chronic sequelae that characterize the long-term morbidity of acute OP-intoxication, including cognitive dysfunction [51], depression [19], and epilepsy [39, 52]. However, there is an absence of studies correlating histological and PET assessments of synaptic density, which we speculate is largely due to the differences in resolution between the modalities. In our study of animals that were assessed by both PET and histology, we observed that approximately 90% of the SV2A

immunoreactive puncta were associated with MAP2 immunopositive processes, suggesting SV2A is predominately synaptic (Supplementary Fig. S8). Additionally, previous studies in rat models observed SV2A IR colocalized more at inhibitory terminals (VGAT) than excitatory terminals (VGLUT1) [47, 53], which is consistent with our observation that approximately 16% of the SV2A immunoreactive puncta colocalized with the excitatory synapse marker PSD95 (Supplementary Fig. S8). This result supports previous claims that increases or decreases observed by SV2A PET may also need to be viewed as changes in the type of neurotransmission [53]. While we found a positive correlation between PET SUV and dendritic spine density at 28 DPE as measured using Golgi staining, we found no significant correlations between PET SUV and synaptic IHC metrics. Differences in the resolution and volume of tissue measured, as well as the scope of these observations may account for the lack of correlation. Additionally, all IHC metrics of synapses were contingent on SV2A IR being associated with MAP2 IR. Although, the restraints of histological techniques do not allow for synaptic density to be measured in human survivors of acute OP intoxication, our results showed significant correlations between histologic and PET measures of synaptic density, suggesting the feasibility of using SV2A PET to screen survivors for changes in synaptic structure.

Collectively, our findings in a rat model of acute OP intoxication indicate an evolving synaptic and dendritic response defined by more robust differences at 10 than 28 DPE. Our data indicate that the acutely observed dendritic regression and synaptic declines does not simply progress to the delayed times post-exposure. However, increased dendritic complexity, decreased cytoskeletal protein IR, and changes in the percentage of dendritic spine maturation describe the dendritic morphology in the weeks to months after acute OP intoxication. Our findings suggest that at delayed times post exposure acute OP-induced effects follow a biphasic response after the early neuronal atrophy, and mechanisms of synaptic plasticity appear to be involved. Additional studies longitudinally assessing dendritic and synaptic effects are necessary to connect the early and late observations in response to acute OP

intoxication, and to determine if a biphasic progression of effects is involved in the mechanism(s) that links the acutely toxic effects of OPs to the development of long-term neurological consequences. Candidate therapies, such as sub-anesthetic administration of Ketamine, have been shown to improve the long term outcomes after acute OP exposure [54, 55], and one possible mechanism responsible for the improvement includes ketamine's ability to promote dendritic arborization in atrophying neurons [56]. Additionally, *in vivo* PET using SV2A targeting radiotracers may be useful for mapping temporal changes in synaptic density following acute OP intoxication, despite the inherent difference in resolution when compared to histological methods. Overall, our data suggests SV2A PET should be explored further as an alternative to histological measures of synaptic changes. The present study was restricted to hippocampal sub-region histological observations and whole hippocampus PET assessments, therefore further studies are needed to evaluate how the temporal pattern we observed may vary in other brain areas or neuronal subtypes, and whether these effects can be modified by therapeutic intervention.

Funding:

This work was supported by the National Institutes of Health CounterACT program [grant number NS079202]. The sponsors were not involved in the study design, the collection, analysis and interpretation of data, the writing of the paper or in the decision to submit the work for publication.

Acknowledgements:

Donald Bruun (dosing and perfusions), James M. Angelastro (antibody validation), Carolyn R. Klocke (histological techniques), Lan Liu (Antibody Validation), Ingrid Brust-Mascher (imaging core).

References:

1. Eddleston, M., et al., *Management of acute organophosphorus pesticide poisoning.* Lancet, 2008. **371**(9612): p. 597-607.
2. Bird, S.B., R.J. Gaspari, and E.W. Dickson, *Early death due to severe organophosphate poisoning is a centrally mediated process.* Acad Emerg Med, 2003. **10**(4): p. 295-8.
3. Jett, D.A., *Neurological aspects of chemical terrorism.* Ann Neurol, 2007. **61**(1): p. 9-13.
4. Gilmore III, J.S. *Reports on the Poisoning of Russian Opposition Leader Aleksey Navalny*. 2020; Available from: https://osce.usmission.gov/reports-on-the-poisoning-of-russian-opposition-leader-aleksey-navalny/.
5. Rojas, A., et al., *Comparison of neuropathology in rats following status epilepticus induced by diisopropylfluorophosphate and soman.* Neurotoxicology, 2021. **83**: p. 14-27.
6. Reddy, D.S. and E. Colman, *A Comparative Toxidrome Analysis of Human Organophosphate and Nerve Agent Poisonings Using Social Media.* Clin Transl Sci, 2017. **10**(3): p. 225-230.
7. Sogorb M, E.J., Vilanova E. , *Toxicokinetics and Toxicodynamics of DFP* Handbook of Toxicology of Chemical Warfare Agents. 2 ed., ed. G. RC. 2015, USA: Elsevier
8. Flannery, B.M., et al., *Persistent neuroinflammation and cognitive impairment in a rat model of acute diisopropylfluorophosphate intoxication.* J Neuroinflammation, 2016. **13**(1): p. 267.
9. Gonzalez, E.A., et al., *The chemical convulsant diisopropylfluorophosphate (DFP) causes persistent neuropathology in adult male rats independent of seizure activity.* Arch Toxicol, 2020. **94**(6): p. 2149-2162.
10. Guignet, M., et al., *Persistent behavior deficits, neuroinflammation, and oxidative stress in a rat model of acute organophosphate intoxication.* Neurobiol Dis, 2020. **133**: p. 104431.
11. Hobson, B.A., et al., *TSPO PET Using [18F]PBR111 Reveals Persistent Neuroinflammation Following Acute Diisopropylfluorophosphate Intoxication in the Rat.* Toxicol Sci, 2019. **170**(2): p. 330-344.
12. Brewster, A.L., et al., *Rapamycin reverses status epilepticus-induced memory deficits and dendritic damage.* PLoS One, 2013. **8**(3): p. e57808.
13. Isokawa, M., *Remodeling dendritic spines in the rat pilocarpine model of temporal lobe epilepsy.* Neurosci Lett, 1998. **258**(2): p. 73-6.
14. Schartz, N.D., et al., *Spatiotemporal profile of Map2 and microglial changes in the hippocampal CA1 region following pilocarpine-induced status epilepticus.* Sci Rep, 2016. **6**: p. 24988.
15. Li, K., et al., *Synaptic Dysfunction in Alzheimer's Disease: Abeta, Tau, and Epigenetic Alterations.* Mol Neurobiol, 2018. **55**(4): p. 3021-3032.
16. Scheff, S.W., et al., *Synaptic alterations in CA1 in mild Alzheimer disease and mild cognitive impairment.* Neurology, 2007. **68**(18): p. 1501-8.
17. Skaper, S.D., et al., *Synaptic Plasticity, Dementia and Alzheimer Disease.* CNS Neurol Disord Drug Targets, 2017. **16**(3): p. 220-233.
18. Duman, C.H. and R.S. Duman, *Spine synapse remodeling in the pathophysiology and treatment of depression.* Neurosci Lett, 2015. **601**: p. 20-9.
19. Holmes, S.E., et al., *Lower synaptic density is associated with depression severity and network alterations.* Nat Commun, 2019. **10**(1): p. 1529.
20. Kang, H.J., et al., *Decreased expression of synapse-related genes and loss of synapses in major depressive disorder.* Nat Med, 2012. **18**(9): p. 1413-7.
21. Abe, H., et al., *Correlation between the surface electronic structure and CO-oxidation activity of Pt alloys.* Phys Chem Chem Phys, 2015. **17**(7): p. 4879-87.

22. Carpentier, P., M. Lambrinidis, and G. Blanchet, *Early dendritic changes in hippocampal pyramidal neurones (field CA1) of rats subjected to acute soman intoxication: a light microscopic study.* Brain Res, 1991. **541**(2): p. 293-9.
23. Zaja-Milatovic, S., et al., *Protection of DFP-induced oxidative damage and neurodegeneration by antioxidants and NMDA receptor antagonist.* Toxicol Appl Pharmacol, 2009. **240**(2): p. 124-31.
24. Farizatto, K.L.G., et al., *Inhibitor of Endocannabinoid Deactivation Protects Against In Vitro and In Vivo Neurotoxic Effects of Paraoxon.* J Mol Neurosci, 2017. **63**(1): p. 115-122.
25. Campana, A.D., et al., *Dendritic morphology on neurons from prefrontal cortex, hippocampus, and nucleus accumbens is altered in adult male mice exposed to repeated low dose of malathion.* Synapse, 2008. **62**(4): p. 283-90.
26. Munirathinam, S. and B.A. Bahr, *Repeated contact with subtoxic soman leads to synaptic vulnerability in hippocampus.* J Neurosci Res, 2004. **77**(5): p. 739-46.
27. Santos, H.R., et al., *Spine density and dendritic branching pattern of hippocampal CA1 pyramidal neurons in neonatal rats chronically exposed to the organophosphate paraoxon.* Neurotoxicology, 2004. **25**(3): p. 481-94.
28. Speed, H.E., et al., *Delayed reduction of hippocampal synaptic transmission and spines following exposure to repeated subclinical doses of organophosphorus pesticide in adult mice.* Toxicol Sci, 2012. **125**(1): p. 196-208.
29. Madeo, M., A.D. Kovacs, and D.A. Pearce, *The human synaptic vesicle protein, SV2A, functions as a galactose transporter in Saccharomyces cerevisiae.* J Biol Chem, 2014. **289**(48): p. 33066-71.
30. Siso, S., et al., *Editor's Highlight: Spatiotemporal Progression and Remission of Lesions in the Rat Brain Following Acute Intoxication With Diisopropylfluorophosphate.* Toxicol Sci, 2017. **157**(2): p. 330-341.
31. Keil, K.P., et al., *In vivo and in vitro sex differences in the dendritic morphology of developing murine hippocampal and cortical neurons.* Sci Rep, 2017. **7**(1): p. 8486.
32. Lein, P.J., et al., *Ontogenetic alterations in molecular and structural correlates of dendritic growth after developmental exposure to polychlorinated biphenyls.* Environ Health Perspect, 2007. **115**(4): p. 556-63.
33. Wilson, M.D., et al., *Valid statistical approaches for analyzing sholl data: Mixed effects versus simple linear models.* J Neurosci Methods, 2017. **279**: p. 33-43.
34. Fiala, J.C., *Reconstruct: a free editor for serial section microscopy.* J Microsc, 2005. **218**(Pt 1): p. 52-61.
35. Risher, W.C., et al., *Rapid Golgi analysis method for efficient and unbiased classification of dendritic spines.* PLoS One, 2014. **9**(9): p. e107591.
36. Li, S., et al., *Synthesis and in Vivo Evaluation of a Novel PET Radiotracer for Imaging of Synaptic Vesicle Glycoprotein 2A (SV2A) in Nonhuman Primates.* ACS Chem Neurosci, 2019. **10**(3): p. 1544-1554.
37. Harris, K.M. and S.B. Kater, *Dendritic spines: cellular specializations imparting both stability and flexibility to synaptic function.* Annu Rev Neurosci, 1994. **17**: p. 341-71.
38. Sadasivam, P., et al., *Quantification of SV2A Binding in Rodent Brain Using [(18)F]SynVesT-1 and PET Imaging.* Mol Imaging Biol, 2021. **23**(3): p. 372-381.
39. Serrano, M.E., et al., *Exploring with [(18)F]UCB-H the in vivo Variations in SV2A Expression through the Kainic Acid Rat Model of Temporal Lobe Epilepsy.* Mol Imaging Biol, 2020. **22**(5): p. 1197-1207.
40. Howard, A.S., et al., *Chlorpyrifos exerts opposing effects on axonal and dendritic growth in primary neuronal cultures.* Toxicol Appl Pharmacol, 2005. **207**(2): p. 112-24.
41. Lein, P.J., et al., *The novel GTPase Rit differentially regulates axonal and dendritic growth.* J Neurosci, 2007. **27**(17): p. 4725-36.

42. Wayman, G.A., et al., *PCB-95 promotes dendritic growth via ryanodine receptor-dependent mechanisms.* Environ Health Perspect, 2012. **120**(7): p. 997-1002.
43. Li, Y., et al., *Spatiotemporal pattern of neuronal injury induced by DFP in rats: a model for delayed neuronal cell death following acute OP intoxication.* Toxicol Appl Pharmacol, 2011. **253**(3): p. 261-9.
44. Swann, J.W. and J.M. Rho, *How is homeostatic plasticity important in epilepsy?* Adv Exp Med Biol, 2014. **813**: p. 123-31.
45. Larner, A.J., *Axonal sprouting and synaptogenesis in temporal lobe epilepsy: possible pathogenetic and therapeutic roles of neurite growth inhibitory factors.* Seizure, 1995. **4**(4): p. 249-58.
46. Represa, A., et al., *From seizures to neo-synaptogenesis: intrinsic and extrinsic determinants of mossy fiber sprouting in the adult hippocampus.* Hippocampus, 1994. **4**(3): p. 270-4.
47. Contreras-Garcia, I.J., et al., *Differential expression of synaptic vesicle protein 2A after status epilepticus and during epilepsy in a lithium-pilocarpine model.* Epilepsy Behav, 2018. **88**: p. 283-294.
48. Wong, M., *Modulation of dendritic spines in epilepsy: cellular mechanisms and functional implications.* Epilepsy Behav, 2005. **7**(4): p. 569-77.
49. O'Brien, R.J., et al., *Activity-dependent modulation of synaptic AMPA receptor accumulation.* Neuron, 1998. **21**(5): p. 1067-78.
50. Rao, A. and A.M. Craig, *Activity regulates the synaptic localization of the NMDA receptor in hippocampal neurons.* Neuron, 1997. **19**(4): p. 801-12.
51. Chen, M.K., et al., *Assessing Synaptic Density in Alzheimer Disease With Synaptic Vesicle Glycoprotein 2A Positron Emission Tomographic Imaging.* JAMA Neurol, 2018. **75**(10): p. 1215-1224.
52. Finnema, S.J., et al., *Reduced synaptic vesicle protein 2A binding in temporal lobe epilepsy: A [(11) C]UCB-J positron emission tomography study.* Epilepsia, 2020. **61**(10): p. 2183-2193.
53. Mendoza-Torreblanca, J.G., et al., *Analysis of Differential Expression of Synaptic Vesicle Protein 2A in the Adult Rat Brain.* Neuroscience, 2019. **419**: p. 108-120.
54. Ribeiro, A.C.R., et al., *Molecular mechanisms for the antidepressant-like effects of a low-dose ketamine treatment in a DFP-based rat model for Gulf War Illness.* Neurotoxicology, 2020. **80**: p. 52-59.
55. Zhu, J., et al., *Assessment of Ketamine and Its Enantiomers in an Organophosphate-Based Rat Model for Features of Gulf War Illness.* Int J Environ Res Public Health, 2020. **17**(13).
56. Ly, C., et al., *Psychedelics Promote Structural and Functional Neural Plasticity.* Cell Rep, 2018. **23**(11): p. 3170-3182.